International Journal of Mechanical Sciences 89 (2014) 65–77

Contents lists available at ScienceDirect

International Journal of Mechanical Sciences

journal homepage: www.elsevier.com/locate/ijmecsci

Design and analysis of pioneering high supersonic axial turbines

G. Paniagua *, M.C. Iorio, N. Vinha, J. Sousa

von Karman Institute for Fluid Dynamics Chaussée de Waterloo 72, 1640 Rhode-Saint-Genèse, Belgium

ARTICLE INFO

Article history:
Received 13 February 2014
Received in revised form
29 July 2014
Accepted 15 August 2014
Available online 27 August 2014

Keywords:
Supersonic flows
Shock wave
Turbine
Starting process

ABSTRACT

The trend towards ultra compact thermal power generation, is constrained by the unavailability of fluid-machinery adequate for supersonic flow conditions. Conventional turbine designs exhibit unacceptable performances related to large aerodynamic losses and a narrow operation range. This paper provides for the first time in the open literature the design procedure, and subsequent analysis of the turbine performance of a turbine adequate for supersonic axial pulsating flows, as those encountered in innovative combustors. The design approach considers the most adverse condition, a steady inlet axial Mach number equal to 3.5. The possible turbine families were classified by the velocity triangles and discussed. A fundamental issue in supersonic passages is to ensure the normal shock at the start of the engine is swallowed through the turbine passages, namely the turbine passage is started. To ensure self-starting capability the turning is restricted to lower values than in the conventional subsonic turbines. The design procedure was based on the method of characteristics, converting the inlet uniform flow into a vortex flow field, such that the adequate deflection is inflicted to the supersonic flow. The performance of the supersonic passage was first assessed and then compared to conventional designs. The present design procedure and analysis of unconventional supersonic turbines provides guidelines for the design and optimization of efficient high supersonic passages, suitable to future tightly packed fluid machinery.

1. Introduction

The thermal efficiency of advanced combined cycles surpasses 62.8%, considering a turbine entry temperature of 1703 K [1]. However, the maximum possible efficiency offered by the Carnot cycle for the same firing temperature would be 82.8%. While further increase in pressure ratios and firing temperature gradually enhance the cycle efficiency, novel turbine-based thermal plants offer a potential leap in efficiency. In particular, the Humphrey and Ficket–Jacobs cycles provide a rise of pressure through the combustion process. Fig. 1a and b display the entropy–enthalpy and pressure–volume charts of the ideal Joule–Brayton (constant pressure heat addition), the Humphrey, and the Ficket–Jacobs cycles. The Humphrey cycle is based on constant volume heat addition with an isentropic expansion and an isobaric heat rejection. In the Fickett–Jacobs cycle, the combustion is an explosive process, utilized in the 1920s in a Hozwarth turbine [2], or using perhaps a special piston-cylinder arrangement, that in practice results in supersonic flow conditions at the combustor exit. A multitude of research teams have suggested the use of pressure gain combustion for power plants [3]. The use of a constant volume combustor, displayed in red in Fig. 1a and b, allows achieving the same time-averaged combustor exit temperature at a higher-pressure level (the turbine inlet temperature T_4 is fixed by the current material technology). Conversely, to achieve the same turbine inlet conditions of a Joule cycle, the Humphrey cycle requires less pressure increase in the compressor. Consequently, the Humphrey cycle offers a potential surge in specific power and cycle efficiency. Nevertheless to achieve the potential gain in such pioneering power plant, the turbine efficiency should be above a certain threshold dictated by the combustor pressure rise and turbine entry temperature. Let us consider that the Joule engine is equipped with a 90% efficiency turbine, Fig. 1c demonstrates that the required efficiency of the turbine in the Humphrey cycle to achieve the same cycle efficiency than the Joule cycle, decreases a function of the combustor pressure rise. Humphrey cycles operating at large turbine entry temperatures, with low compression ratio require low turbine efficiencies. For instance, in a Humphrey cycle with $T_4 = 1500$ K, $P_3/P_2 = 5$, with a combustor pressure rise of 40%, a turbine with an isentropic efficiency of 59% would extract the same work than a 90% efficiency turbine in a Joule cycle.

The fulcrum in the practical implementation of energy conversion based on those unprecedented cycles is the lack of fluid machinery adequate to cope efficiently with the combustor exit supersonic flows. The interaction of conventional turbines, designed for subsonic axial flow, with transient supersonic inlet flows has resulted in unacceptably deficient aerodynamic performance, below 30% [4], that prevents a satisfactory thermoeconomic comparison with state-of-the art thermal cycles [1].

* Corresponding author. Tel.: +32 476443405.
E-mail address: gpaniagua@me.com (G. Paniagua).

http://dx.doi.org/10.1016/j.ijmecsci.2014.08.014

Nomenclature

A	Area [m^2]
C	Chord [m]
C_p	Specific heat capacity at constant pressure [J/kg K]
e	Relative error
g	Pitch [m]
H	Specific enthalpy [J/kg]
L	length [m]
LE	Leading edge
M	Mach number $V/(\gamma.\Re.T)^{1/2}$
$\dot{m}$	Mass flow [kg/s]
N	Number of grid cells
r	Grid refinement factor
R	Radius [m]
$\Re$	Ideal gas constant [J kg^{-1} K^{-1}]
P	Pressure [Pa]
s	Entropy [J/K]
T	Temperature [K]
t	Time [s]
U	Peripheral velocity [m/s]
V	Velocity in the absolute frame of reference [m/s]
W	Velocity in the relative frame of reference [m/s]
x	Length along the axial direction [m]
y	Length along the tangential direction [m]
y^+	Normalized distance of first wall cell

Greek symbols

α	Absolute flow angle from the axial direction, positive in the sense of rotor turning [deg]
β	Relative flow angle from the axial direction, positive in the sense of rotor turning [deg]
γ	Specific heat ratio
δ	Wedge angle [deg]
φ	Velocity direction
Δ	Difference
θ	Tangential displacement [rad]
ν	Prandtl–Meyer angle [deg]
μ	Dynamic viscosity [Pa s]
ω	Rotational velocity [rad/s]

Subscripts

r	Relative frame of reference
s	Static quantities
0	Total quantities
1,2	Inlet and outlet conditions of a stator row, respectively
2,3	Inlet and outlet conditions of a rotor row, respectively

Moreover, pulsating high-speed flows are also encountered at the inlet of the radial turbines used in supercharged combustion engines [5]. Alas, there is no public literature on how to design turbines operating at supersonic axial inlet flows. The available literature is restricted to airfoils exposed to subsonic axial conditions.

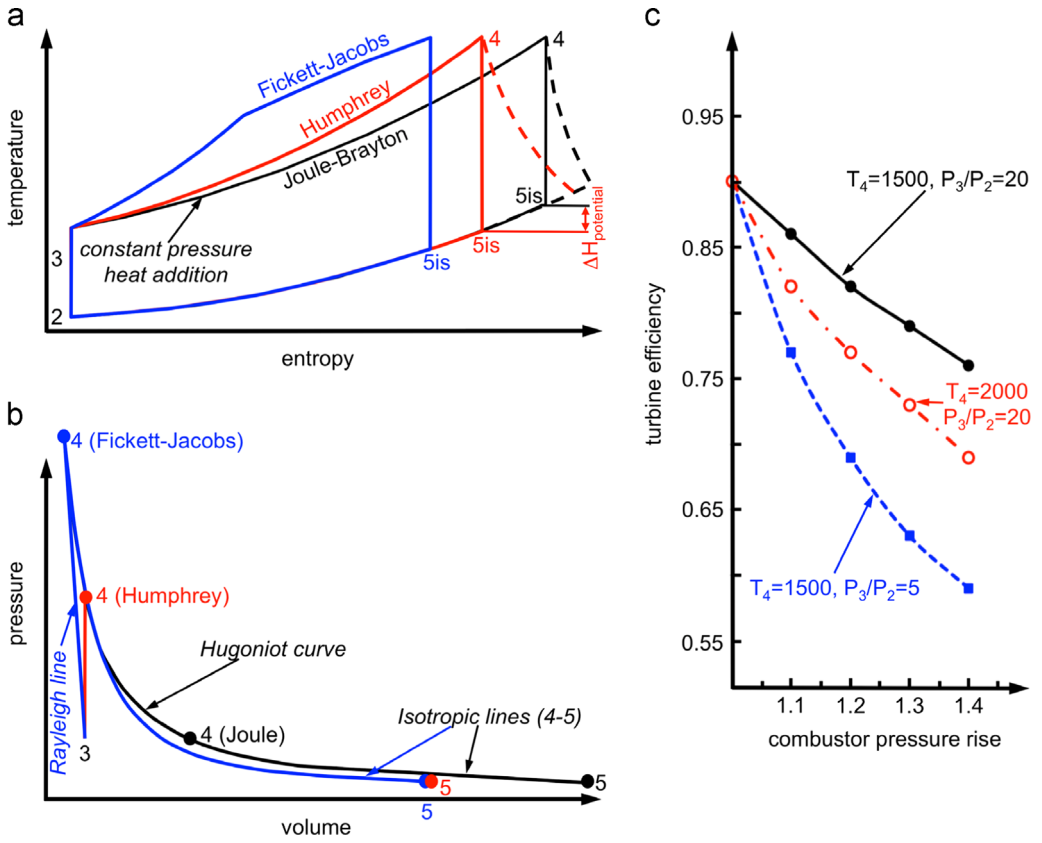

Fig. 1. Single closed loop cycles: a) Simplified enthalpy–enthropy representation; b) Pressure–volume layout; c) Turbine efficiency in a Humphrey cycle to obtain the same efficiency than a Brayton cycle with a 90% turbine efficiency.(For interpretation of the references to color in this figure, the reader is referred to the web version of this article.)

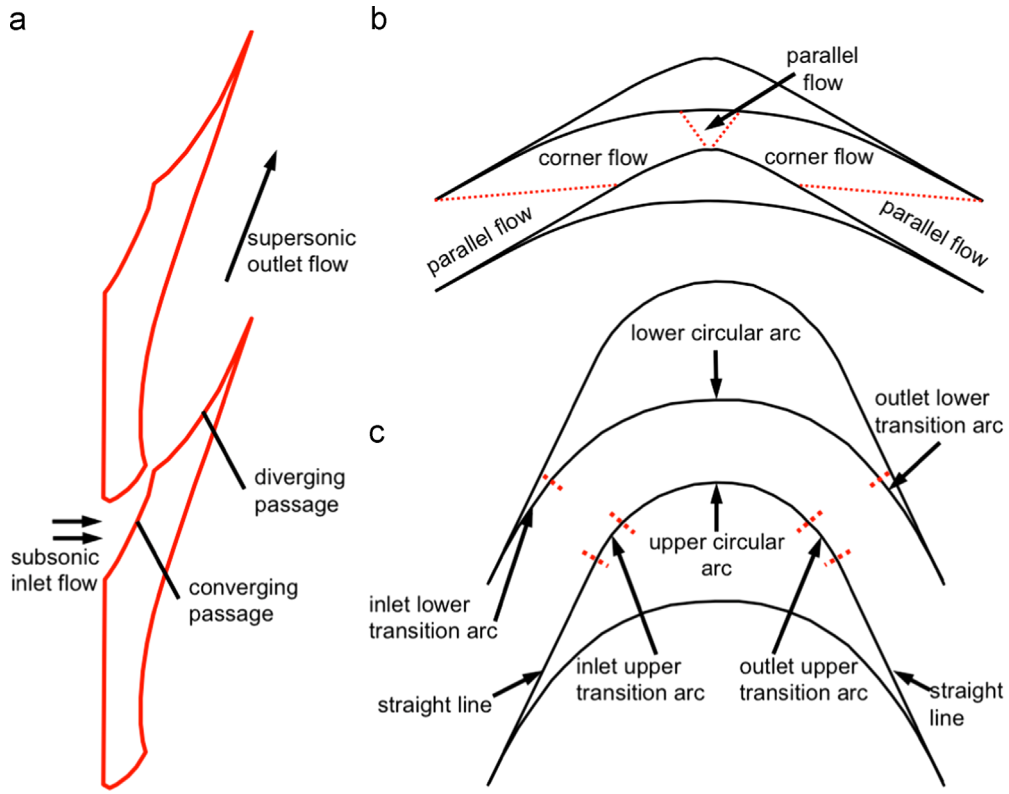

Fig. 2. Supersonic passage designs: a) nozzle design for a subsonic inlet flow; b) rotor design by the corner-flow method; c) rotor design with vortex flow field.

Supersonic turbines have attracted interest from the industry since the 1950s due to the high specific power they could provide, allowing a reduction in the number of low-pressure stages, and thus leading to lighter turbines together with lower manufacture and operational costs. Verneau, and Verdonk and Dufournet [6] presented supersonic turbines designed for solar plants, waste energy recovery, and for a turbo-generator. Wahlen [7] demonstrated the use of supersonic turbines in rocket engines that are currently in use. Supersonic outlet axial stators are considered in large diesel engines to achieve more compact turbochargers [8]. All the preceding turbine stages include a converging–diverging nozzle, to accelerate the flow from an inlet subsonic axial velocity up to a supersonic, high turning flow. Goldman and Vanco [9] developed a method to design sharp-edged-throat supersonic nozzles that deliver a uniform parallel flow at the nozzle exit. Fig. 2a depicts three distinct regions in the vane nozzle: a converging (subsonic) section, a diverging (supersonic) section and a straight section in the rear suction surface. To maximize the specific power, the degree of reaction is traditionally very low. The design of such impulse type rotors can be achieved following two different strategies based on the method of characteristics [10]:

- Fig. 2b shows a passage designed with the "corner flow method" [11]. The front suction side is curved to cancel the incoming compression waves generated along the concave pressure side, followed then by a parallel flow. The flow subsequently experiences a corner flow expansion, where waves are canceled by the concave surface, until uniform parallel flow is achieved at the exit. However, the design exhibits zero loading in the central part of the passage, and the flow turning is limited.
- Fig. 2c displays a passage based on the "vortex flow method" [12], where the inlet parallel flow is converted into a vortex flow field with the proper design of inlet transition arcs. Then through circular arcs the flow is turned, and finally the outlet transition arcs provide a uniform parallel outlet flow [13]. This design favors high turning and loading.

When convergent passages are submitted to supersonic axial inlet conditions, the resulting supersonic diffuser may become *unstarted*, namely a normal shock appears at the turbine inlet passage, as presented in Fig. 3-left. Kantrowitz and Donaldson [14] demonstrated that the starting capability of a supersonic diffuser is essentially driven by two parameters: the inlet Mach number (M_{inlet}) and the area ratio between the inlet and the throat. Fig. 3-right shows the isentropic limit to supersonic flows as defined by Eq. (1) for a certain inlet Mach number.

$$\frac{A_{throat}}{A_{inlet}} = \frac{1}{M_{inlet}}\left(\frac{2(1+(\gamma-1)/2)M_{inlet}^2}{\gamma+1}\right)^{-(\gamma+1)/(2(\gamma-1))} \tag{1}$$

However Eq. (1) does not ensure a *self-starting* design, viz., a bow shock cannot be stable in front of the supersonic diffuser but is instead swallowed. If the turbine is able to ingest the normal shock that occurs at the inlet of the airfoil passage during the start-up, it is considered to be *self-started*. In order to determine this area ratio one needs to reevaluate the isentropic limit Eq. (1) using as inlet Mach number (M_{inlet}) the actual Mach number at the turbine inlet, i.e. downstream of a normal shock (M_2) with Eq. (2):

$$M_2^2 = \frac{(\gamma-1)M_{inlet}^2+2}{2\gamma M_{inlet}^2-(\gamma-1)} \tag{2}$$

When the bow shock is attached to the passage without flow spillage, the turbine passage can start but never spontaneously, and is considered to be the *critical mode*. The self-starting region (above the Kantrowitz line, blue solid line in the Fig. 3-right) limits the amount of possible turning in a supersonic inlet cascade. The accurate prediction of the starting Mach number is intricate, depending on the local passage Mach number and boundary layer thickness [15].

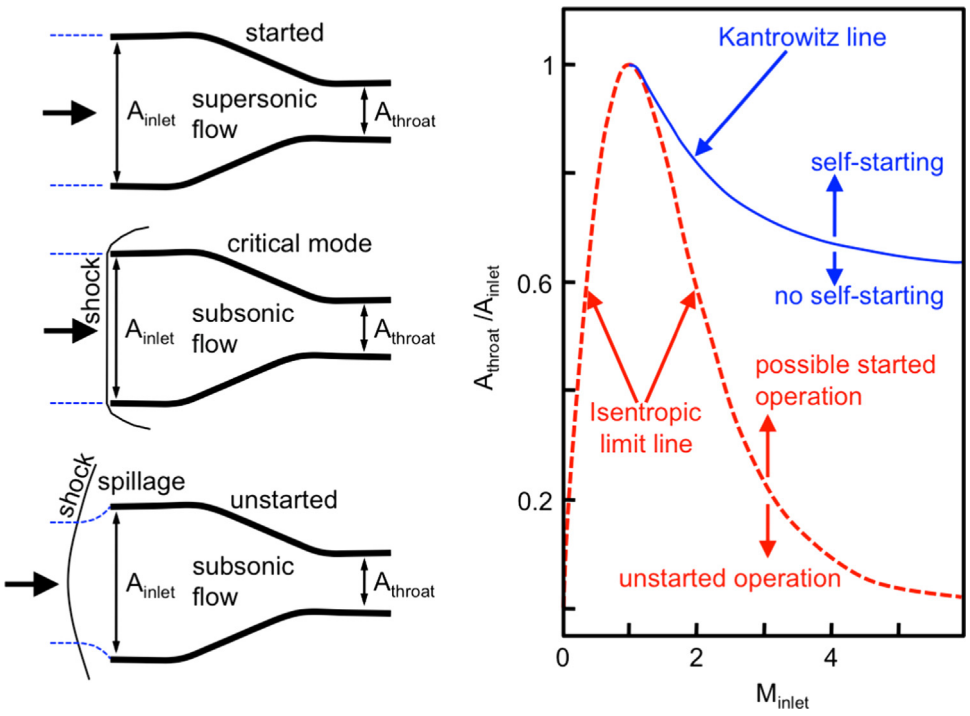

Fig. 3. Possible intake operating regions: The red dashed line marks the isentropic limit between started (above the line) and the unstarted region (below the line). The blue solid line indicates the Kantrowitz line between the *self started* (above the line) and *not self started* (below the line).(For interpretation of the references to color in this figure legend, the reader is referred to the web version of this article.)

State-of-the-art high-pressure-turbine vane passages are characterized by a strong area contraction up to the throat. Consequently, when conventional vanes are exposed to high supersonic inlet Mach numbers the diffuser is never self-starting. Standing shock waves upstream of the turbine cascade cause large irreversibilities and, in particular, abatement of the dynamic pressure. The higher is the inlet Mach number the higher are the total pressure losses. Fig. 4 shows that at an inlet Mach number of 3.5 the total pressure decrease across a normal shock wave is about 78%. However, if one could get a started solution, with oblique shock waves originated at the leading edge, the decrease in total pressure would be considerably smaller. The change of total pressure across oblique shock waves is a function of the inlet Mach number and the wedge angle of the airfoil. Considering a wedge angle of 20° and an inlet Mach number of 3.5, the total pressure abatement would be only 23%, i.e. there would be 3.3 times fewer losses than across a normal shock wave. Clearly a started passage offers a larger potential to extract useful power.

An additional problem is the unfavorable pressure gradient across supersonic diffusers that may lead to boundary layer separation, which additionally limits flow turning in the passage. Furthermore, the efficiency of a supersonic turbine is seriously penalized by the existence of flow separation on the suction surface caused by shock–boundary layer interactions. Higher loadings, i.e. higher suction surface Mach numbers and lower pressure surface Mach numbers are desirable for the starting condition [14] as well as to maximize the work produced by the turbine. However, adverse pressure gradients will become much more pronounced within the passage, clearly showing an important compromise between starting conditions and flow separation.

The current paper presents an approach to design turbine passages with adequate contraction area ratios. The performance of these unconventional turbine passages was evaluated numerically using the solver CFD++, both in steady and transient operation, to study the movement of a normal shock wave across the turbine. The fundamental purpose of the present research is to provide guidelines to designers of an unprecedented family of turbine passages suitable for supersonic applications. In addition, the performance analysis of the components is needed to assess the potential performance gain of novel thermal cycles operating with internal supersonic flows.

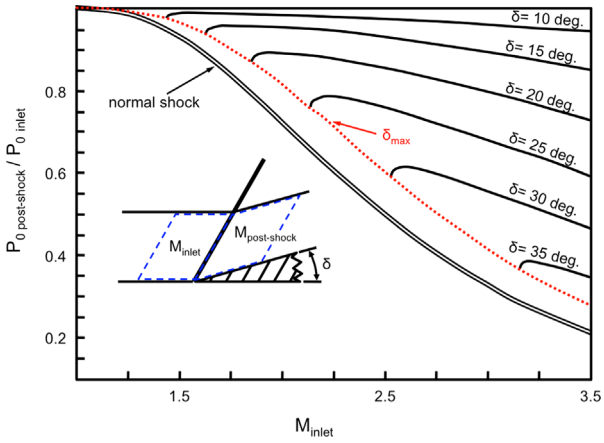

Fig. 4. Total pressure across a normal shock and oblique shocks for various wedge angles (δ) of 10–35°.

2. Turbine design procedure

2.1. Possible turbine architectures with supersonic axial inlet conditions

Fig. 5 displays all the possible turbine configurations considering an axial supersonic inlet flow, the velocity triangles and the associated entropy–enthalpy diagrams. Considering adiabatic conditions, without cooling, the turbine channel outlet static conditions can be evaluated using the compressible flow equations,

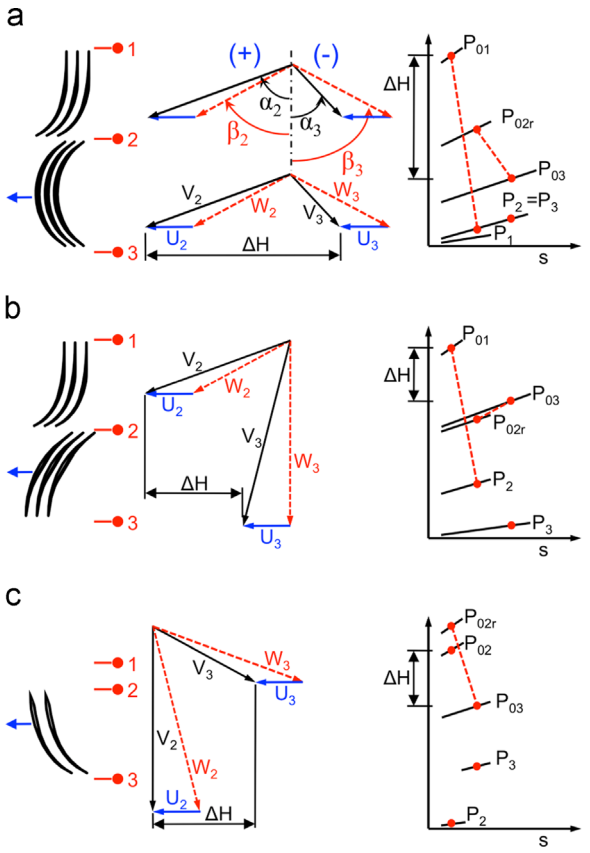

Fig. 5. Velocity triangles and entropy–enthalpy diagrams of the three possible supersonic turbine configurations: a) low reaction turbine both stator and rotor with diffusing channels; b) reaction turbine, rotor with a nozzle design; c) statorless configuration with diffusing geometry. Angles are defined relative to the axial direction, positive in the sense of rotor turning.

corresponding to a stator or rotor passage by applying the mass conservation principle:

$$\frac{\dot{m}\sqrt{C_pT_0}}{A_nP_0}=\frac{\gamma}{\sqrt{\gamma-1}}M\left(1+\frac{\gamma-1}{2}M^2\right)^{-(\gamma+1)/(2(\gamma-1))} \tag{3}$$

Within an axial turbo machine the pitch (g) is constant, assuming a constant channel height (H), the area ratio inlet to any station (A_n/A_{inlet}) can be expressed according to the following expression Eq. (4):

$$\frac{A_n}{A_{inlet}}=\frac{H\cdot g\cdot cos(\alpha_n)}{H\cdot g\cdot cos(\alpha_{inlet})}=\frac{cos(\alpha_n)}{cos(\alpha_{inlet})} \tag{4}$$

Neglecting pressure losses and assuming constant flow properties, the mass flow conservation across the passage yields the outlet Mach number (M_{outlet}) as a function of the inlet Mach number (M_{inlet}) and the passage turning as shown by Eq. (5). For a stator the equation is terms of the absolute angle ($\alpha_{outlet}-\alpha_{inlet}$), while for a rotor the turning would be expressed in the relative frame of reference ($\beta_{inlet}-\beta_{outlet}$):

$$\left(1+\frac{\gamma-1}{2}M_{inlet}^2\right)^{-(\gamma+1)/(2(\gamma-1))}M_{inlet}cos\alpha_{inlet}$$
$$=\left(1+\frac{\gamma-1}{2}M_{outlet}^2\right)^{-(\gamma+1)/(2(\gamma-1))}M_{outlet}cos\alpha_{outlet} \tag{5}$$

Flow turning results in an area contraction; in turbines with axial inlet flow, the turbine vane behaves as supersonic diffuser. One can then consider two types of stator-rotor turbine configurations, an impulse design, low reaction, Fig. 5a with a rotor-diffusing channel, and a reaction concept as sketched in Fig. 5b with a rotor nozzle design. The work extraction is maximum for a vane outlet swirl equals to 67° and rotor turning equals to 116° ($\beta_2=\beta_3=58°$), implying no velocity change across the rotor passage if there were no shock losses. This impulse design (Fig. 5a) delivers a high outlet swirl, and both stator and rotor passages experience diffusion. In the rotor relative frame of reference, due to the upstream stator and peripheral velocity of the passage, inlet swirl to the rotor is present, hence flow acceleration is possible across the rotor passage. Fig. 5b depicts the velocity triangle of a turbine that comprises rotor passages with flow acceleration (nozzle type). Such a design would be the most benign for the rotor aerodynamics, however the work extraction is limited. An alternative solution, with a similar work extraction, would be to consider a stator-less configuration, as sketched in Fig. 5c. The rotor is diffusing the flow, but such a concept offers numerous advantages, particularly a reduction in the number of components. In the following the design is concerned with either the stator geometry displayed in Fig. 5a and b or the rotor of Fig. 5c.

2.2. Vortex flow field design approach

In steady supersonic flows the governing equations are hyperbolic, being the flow properties at each point independent of the downstream conditions. Hence, marching-type numerical methods like the Method of Characteristics can be applied. Fig. 6 displays a turbine passage composed of three regions: inlet transition arcs (D to C and B to A) that converts the inlet uniform flow into a vortex flow; concentric circular arcs (downstream of C along the pressure side, and downstream of A along the suction side) are used to turn and maintain the vortex flow [13]; and outlet transition arcs to transform the flow back into uniform conditions at the exit.

Characteristic lines divide the flow field into several regions, where the flow properties are assumed to be constant. A MATLAB code using a method of characteristics was developed to convert the uniform parallel flow at the airfoil inlet into a vortex flow field, such that the adequate deflection is inflicted to the supersonic flow. The inlet Mach number (M_{inlet}) is reduced to the pressure side level (M_{lower}) and increased to the suction side level (M_{upper}) through the transition arcs. The transition arcs are made of a sequence of straight-line wall segments that change with the flow direction, intersecting the straight Mach lines every flow turning's variation.

When considering isentropic flow turning at supersonic speeds the required flow deviation to achieve a targeted Mach number can be evaluated through the Prandl–Meyer angle as defined in Eq. (6). This value represents the angle through which the flow

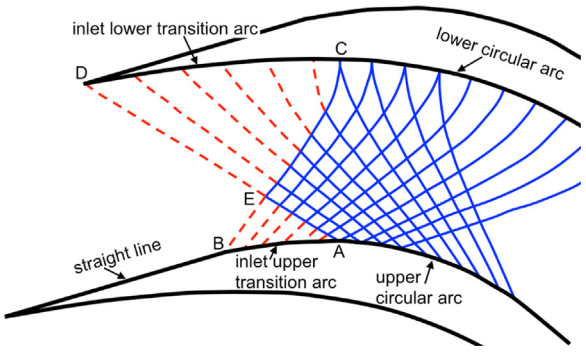

Fig. 6. Characteristic lines within the passage.

must turn from $M=1$ to the required Mach number.

$$\nu=\frac{\pi}{4}\left(\sqrt{(\gamma+1)/(\gamma-1)}-1\right)+\frac{1}{2}\left\{\sqrt{(\gamma+1)/(\gamma-1)}\sin^{-1}\left[(\gamma-1)M^{*2}-\gamma\right]+\sin^{-1}\left(\frac{\gamma+1}{M^{*2}}-\gamma\right)\right\} \quad (6)$$

The critical velocity ratio M^* is expressed by the following relation Eq. (7):

$$M^*=\left(\frac{M^2(\gamma-1)/2}{1+M^2(\gamma-1)/2}\right)^{1/2} \quad (7)$$

Hence, the flow turning produced by the transitional arcs is determined by the targeted Mach number in the upper side (M_{upper}) and in the lower side (M_{lower}) at point A and C in Fig. 6 along the circular arc region. Therefore, considering a certain inlet Mach number (M_{inlet}) the flow turning must be equal to the differences in the Prandlt–Meyer angles, $\nu_{inlet}(M_{inlet})-\nu_{lower}$ (M_{lower}) for the lower side and $\nu_{upper}(M_{upper})-\nu_{inlet}(M_{inlet})$ for the upper side. The circular arcs are designed to maintain the vortex flow field region, where the flow velocity is inversely proportional to the radius:

$$V\cdot R=\text{constant} \quad (8)$$

Therefore, the pressure and suction side Mach numbers remain constant along the vortex region. When normalizing Eq. (8) by the critical velocity ($V_{critical}$) and the correspondent radius of the sonic velocity streamline (r^*) it can be re-written with dimensionless parameters (at $R=r^*$, $V=V_{critical}$):

$$M^*\cdot R^*=1 \quad (9)$$

Where $R^*=R/r^*$ is the dimensionless radius of the vortex flow field and $M^*=V/V_{critical}$ is the dimensionless velocity. Once the designer specifies the values for ν_{upper} and ν_{lower}, the values of $M_{upper}{}^*$ and $M_{lower}{}^*$ are fixed and $R_{upper}{}^*$ and $R_{lower}{}^*$ can be determined with Eq. (9). Considering β_{inlet} and β_{outlet} as the inlet and outlet flow angles respectively, the amount of turning in the circular arcs region are defined by Eq. (10).

$$\begin{aligned}\alpha_{lower,inlet}&=\beta_{inlet}-(\nu_{inlet}-\nu_{lower})\\ \alpha_{lower,outlet}&=\beta_{outlet}-(\nu_{outlet}-\nu_{lower})\\ \alpha_{upper,inlet}&=\beta_{inlet}-(\nu_{upper}-\nu_{inlet})\\ \alpha_{upper,outlet}&=\beta_{outlet}-(\nu_{upper}-\nu_{outlet})\end{aligned} \quad (10)$$

In order to fully define the circular arcs, the outlet flow angle β_{outlet} is determined with Eq. (5), for a selected outlet Mach number (M_{outlet}). Since the starting and terminal points are known, the circular arcs are now fully defined. The design of the lower transitional arcs is performed with respect to non-dimensional axes $x^*=x/r^*$ and $y^*=y/r^*$. The arcs are designed in a marching manner by adding straight wall segments that produce a small change in the flow angle and the respective variation in the Mach number. According to [12] the velocity direction (φ) can be written in function of the dimensional radius.

$$\varphi=\pm\frac{1}{2}f(R^*)+const. \quad (11)$$

$$f(R^*)=\sqrt{(\gamma+1)/(\gamma-1)}\sin^{-1}\left(\frac{(\gamma-1)}{R^{*2}}-\gamma\right)+\sin^{-1}((\gamma-1)R^{*2}-\gamma) \quad (12)$$

The positive sign in Eq. (11) stands for the expansion lines, while the negative sign represents the compression lines. Applying a known boundary condition at $x^*=0$ where $\varphi=0$ and $R^*=R_{lower}{}^*$, the equation for the expansion lines is defined by Eq. (13).

$$\varphi=\frac{1}{2}[f(R^*)-f(R_l^*)] \quad (13)$$

Considering now the discretization of the transition arc into k segments where each one turns the flow in $\Delta\nu$ degrees it is possible to determine the direction of each one of them with Eq. (14).

$$\varphi_{k,inlet}=\nu_{inlet}-\nu_{lower}-(k-1)\Delta\nu \quad (14)$$

This definition of φ can now be used in Eq.(13):

$$f(R_k^*)=2\nu_{inlet}-2(k-1)\Delta\nu-2\nu_{lower}+f(R_{lower}^*) \quad (15)$$

Substituting now the two last terms into Eqs. 6 and 12, the value of $f(R_k{}^*)$ becomes only in function of the dimensionless radius and the incremental flow turning as shown in Eq. (16).

$$f(R_k^*)=2\nu_{inlet}-2(k-1)\Delta\nu-\left(\frac{\pi}{2}\sqrt{(\gamma+1)/(\gamma-1)}-1\right) \quad (16)$$

Eqs. 12 and 17 allow the determination the values of $R_k{}^*$ and φ_k. Hence for each k increment its coordinates can be determined with Eq. (17).

$$x_{k,inlet}^*=-R_{k,inlet}^*\sin\varphi_{k,inlet}^* \quad (17)$$

$$y_{k,inlet}^*=R_{k,inlet}^*\cos\varphi_{k,inlet}^*$$

Each segment of the transitional arc is a straight line parallel to the velocity direction φ_k, therefore the slope of the wall m_k can be computed with Eq. (18)

$$m_{k,inlet}=\tan\varphi_{k+1,inlet}^* \quad (18)$$

Finally the equation of the wall segment can be determined, where k varies from 1 to $k_{max}=(\nu_i-\nu_l)/\Delta\nu$.

$$y^*=m_{k,inlet}\left[x^*-(x_{lower}^*)_{k+1,inlet}\right]+(y_{lower}^*)_{k+1,inlet} \quad (19)$$

The design methodology of the upper transitional arc is analogous to the one used for the lower transitional arc. At the outlet of the passage the procedure is reversed to achieve the uniform outlet Mach number (M_{outlet}). The remainder of the airfoil design is thereby completed with the use of straight lines, on the suction surface, parallel to the flow direction.

2.3. Sharp airfoil designs

Table 1 lists the entry conditions to the supersonic difussing passage, either the vane in Fig. 5a and b or the rotor passage in Fig. 5c (relative inlet conditions). The turbine passage was at first constrained by hub and tip end-walls at constant diameter, with a height equal to 50 mm, a mean diameter of 369.85 mm, and 23 airfoils, which results in about 100 mm of pitch at mid-span.

The characteristics of the four designed passages are listed in Table 2. From airfoil A–D, the turning is reduced, as is consequently the contraction ratio, which results in an increase of the outlet Mach number. For all the airfoils the outlet Mach number is lower than at the inlet, which is related to a higher outlet static pressure than at the inlet ($P_{s\ outlet}>P_{s\ inlet}$). Passages A, B and C display a contraction ratio below the Kantrowitz line, thus such supersonic diffuser is not able to self-start. To circumvent this problem, the meridional airfoil profile for passage A was modified, by increasing the outlet radius at tip, and reducing the outlet radius at the hub (the exit passage height is 70 mm) to allow a self-starting situation.

Table 1
Inlet conditions to the supersonic passage.

M_{inlet}	3.5
α_{inlet} [deg]	0.0
$P_{0\ inlet}$ [bar]	40
$P_{s\ inlet}$ [bar]	0.52
$T_{s\ inlet}$ [K]	725

Table 2
Supersonic passages outlet properties.

	M_{outlet}	$P_{s\ outlet}$ [bar]	α,β_{outlet} [deg]	ν_{upper} [deg]	ν_{lower} [deg]	A_{throat}/A_{inlet}
A	2.5	2.3	67	82	38	0.45
B	2.8	1.5	59	74	40	0.52
C	3.0	1.1	51	78	38	0.61
D	3.4	0.6	24	66	46	0.80

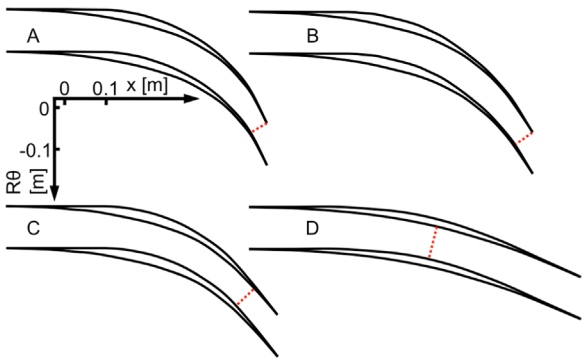

Fig. 7. The sharp airfoils A, B, C, and D, with the throats marked with red dotted lines. (For interpretation of the references to color in this figure legend, the reader is referred to the web version of this article.)

Fig. 7 shows the geometry of the four different passages. In cases A and B, the throat is located at the trailing edge, while for airfoils C and D the throat is located upstream. The numerical simulations demonstrated that for all geometries a constant Mach number region exists as defined with the design approach based on the Method of characteristics. Reducing the turning (from airfoil A to airfoil D) we decrease the pressure loading on the airfoil and the contraction ratio. In this research the airfoil height was kept constant in order to focus on the 2D blade-to-blade analysis and ease the practical implementation in a stator row (with a given diameter) and control the tip radius in a rotating row. Consequently, airfoil D was selected to ensure self-starting of the passage during the testing of the cascade from no-flow into the supersonic regime.

2.4. Reshaping leading and trailing edges

In order to allow for the required internal cooling, the airfoils cannot have sharp edges. Furthermore, regarding structural issues, one cannot allow very narrow leading and trailing edges. Therefore, in the present research both the leading and trailing edges were designed with circular arcs of 5 mm in diameter. The final airfoil design, with the details of the leading and trailing edges, is presented in Fig. 8. A future optimization of the airfoil should comprise the conflicting objectives of aerodynamic performance, structural and thermal integrity. The optimization could then be based on a multi-stage approach as that developed by Joly et al. [16], completed with high-fidelity aero-thermo-mechanical performance considering simultaneously Computational Fluid Dynamics and Computational Structural Mechanics.

2.5. Three dimensional geometry of the turbine passage

The three dimensional annular row contains 23 cylindrical uncooled airfoils with the characteristics listed in Table 3. The airfoil stagger angle is 12° with an outlet metal angle of 24°. The uncooled cylindrical airfoil was obtained by radial stacking of the designed 2-D mid-section, the stacking line is the vector radius

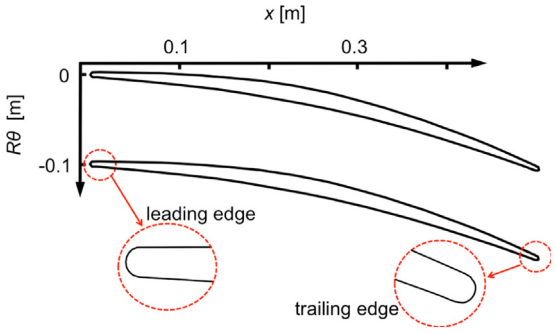

Fig. 8. Airfoil with rounded leading and trailing edges.

Table 3
Turbine passage design characteristics.

Number of airfoils	23		
Height [m]	0.050		
	hub	mid-span	tip
Chord [m]	0.562	0.562	0.562
Axial chord [m]	0.550	0.550	0.550
Inlet radius [m]	0.345	0.370	0.392
Outlet radius [m]	0.345	0.370	0.392
Pitch [m]	0.094	0.101	0.108
Throat [m]	0.075	0.081	0.086
Trailing edge thickness [m]	0.005	0.005	0.005

along the leading edge. The airfoils are considered to be without any tip gap, representative of a stator row, or shrouded rotor row.

3. Numerical calculation

3.1. Governing equations and solver settings

The Reynolds-averaged Navier–Stokes equations were solved with the one-equation Spallart–Almaras turbulence model. In the numerical simulations the fluid is assumed to be a thermally and calorically perfect gas. The turbulence intensity level at the inlet was set at 5%. The CFD++ solver, developed and validated by Metacomp Technologies in the subsonic and transonic range [17], was also assessed and validated at the von Karman Inistitute for hypersonic flows [18]. This solver applies the finite volume method for the spatial discretization, with all control volumes being cell-centered. The inviscid flux function was a second-order, upwind scheme. In order to solve the governing equations, a coupled density-based algorithm has been chosen. The first/second-order blending technique was used to accelerate convergence. However, all solutions were achieved using second order discretization. The temporal discretization scheme used for the computations is a second-order accurate, point-implicit time integration scheme with multi-grid relaxation and a local time-stepping technique, defined by the Courant–Friedrichs–Lewy (CFL) number. CFD++ allows an automatic CFL adjustment procedure when a time-step is too large, in order to avoid numerical instabilities and solution divergence. This technique decreases the CFL to lower values during strong transients, but allows the time-step to increase later.

3.2. Numerical tool validation

A validation of CFD++ was performed on a canonical case, the backward facing step documented by Smith [19] at an inlet Mach

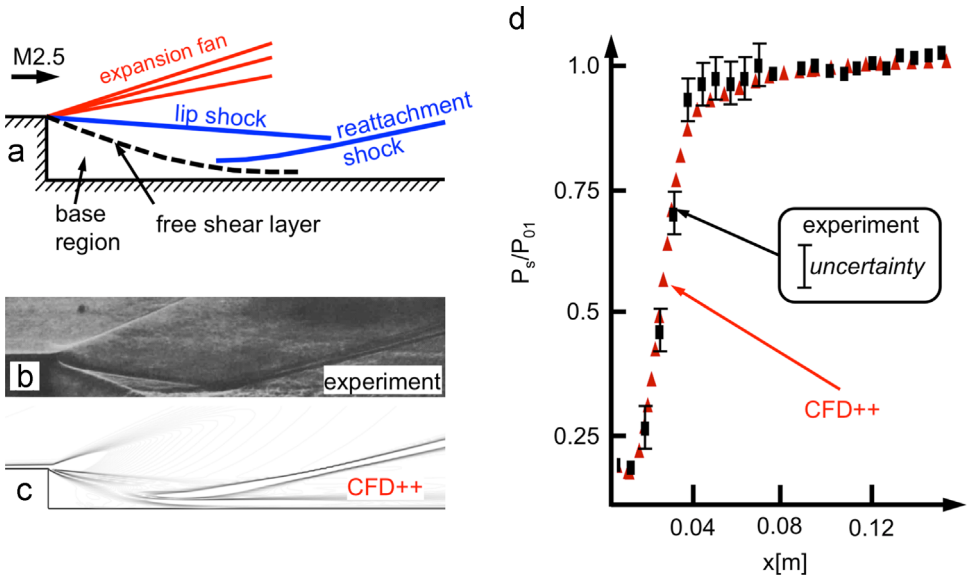

Fig. 9. (a) Main flow features in the supersonic backward facing step, (b) experimental shadowgraph [19], (c) shadowgraph obtained with CFD++ and (d) static pressure distribution downstream of the backward facing step.

Table 4
Results of grid sensitivity analysis.

	$\phi = P_{0\ outlet}/P_{0\ inlet}$ [−]	$\phi = M_{outlet}$ [−]	$\phi = P_{s\ outlet}$ [Pa]
$N_{fine}/N_{medium}/N_{coarse}$	6,215,398 / 2,117,502 / 721,966		
$r_{medium\text{-}fine}$ / $r_{coarse\text{-}medium}$	1.43 / 1.43		
ϕ_{fine} / ϕ_{medium} / ϕ_{coarse}	0.42 / 0.41 / 0.41	2.29 / 2.28 / 2.27	118,570 / 118,621 / 119,309
p	4.34	2.04	7.26
$\phi_{extrapolation}^{medium\text{-}fine}$	0.42	2.30	118,566
$e_a^{medium\text{-}fine}$	2.60%	0.57%	0.04%
$e_{extrapolation}^{medium\text{-}fine}$	0.69%	0.53%	0.00%
$GCI_{fine}^{medium\text{-}fine}$	0.87%	0.66%	0.00%

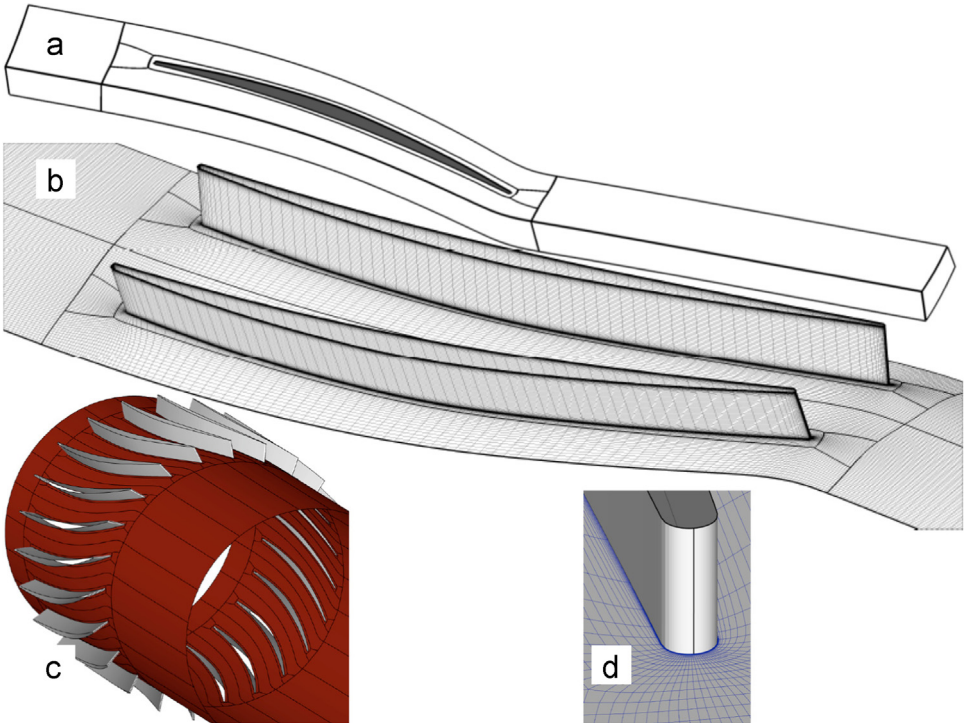

Fig. 10. (a) Topology of the structural blocks used to mesh a single passage; b) Computational grid on the hub and airfoil; c) Three dimensional view of the 3D row; d) Detail of the leading edge grid.

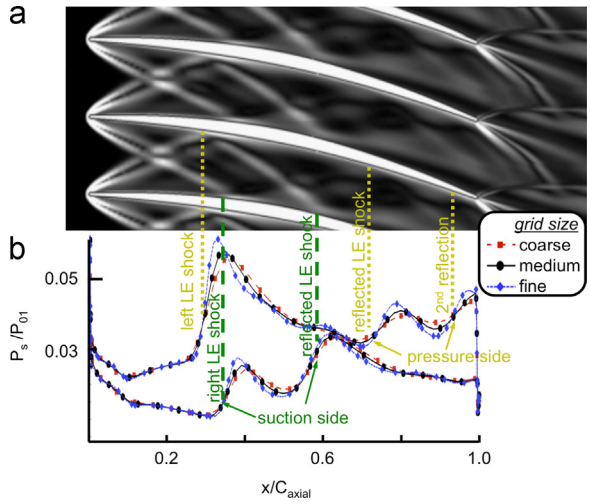

Fig. 11. (a) Numerical Schlieren visualization of the shock waves. b) Static pressure distribution at mid-span for the three grids (*coarse*, *medium and fine*).

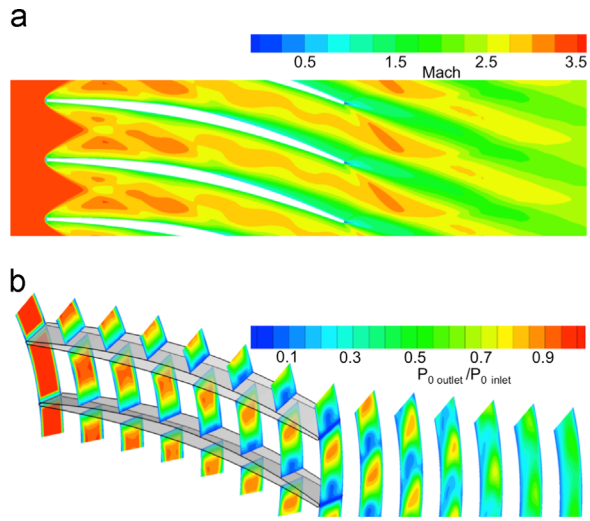

Fig. 12. (a) Mach number contour plots at mid-span. b) Total pressure ratio ($P_{0\ outlet}/P_{0\ inlet}$) across the turbine passage.

number of 2.5, inlet total pressure of 2.275 bar, and inlet total temperature of 344 K. The geometry has a 0.0113 m step, a 0.1016 m upstream section and 0.3048 m downstream segment. The y^+ (as defined by Eq. (20)) all along the lower wall was set to allow an accurate resolution of the laminar sublayer. The resulting 2D mesh had 44118 grid points.

$$y_{wall} = 6\left(\frac{V_{reference}}{\frac{\mu}{\rho}}\right)^{\frac{-7}{8}}\left(\frac{L_{reference}}{2}\right)^{\frac{1}{8}} y^+ \tag{20}$$

Fig. 9(a) sketches the main flow pattern in this supersonic backward facing step. The upstream boundary layer detachment generates a shear layer between the upper supersonic flow and the lower subsonic recirculation (base region), which gives rise to a Prandtl–Meyer expansion fan, and a lip shock. At the confluence of the shear layer with the lower wall an intense reattachment shock appears. Fig. 9b and c shows that differences between the experimental and CFD++ shadowgraphs are negligible. Fig. 9d presents the static pressure distribution along the axial direction, downstream of the step. The CFD++ data are within the experimental uncertainty, represented with a vertical band. The base pressure, length of the separation bubble and the strength of the recompression shock are accurately computed with CFD++.

3.3. Computational grid

The software AutoGrid5, developed by Numeca, was used to generate a three-dimensional, structured multi-block grid. The first step consists of the generation of flow paths or approximate streamlines in the meridional plane. These flow paths define the meridional trace of the surfaces of revolution necessary to build the three-dimensional grid. The following step is the generation of two-dimensional airfoil-to-airfoil meshes (of type HHOHH), at several span-wise positions.

Fig. 10a and b shows the final seven-block structured mesh per passage created by stacking the meshes around airfoil sections. Fig. 10d depicts the leading edge block. The final grid contained 2,117,502 grid cells for two airfoil passages, with boundary layer refinement to ensure y^+ as defined by Eq. (20) values lower than 1 at the walls, with a maximum expansion ratio of 1.1 for the cells near the walls.

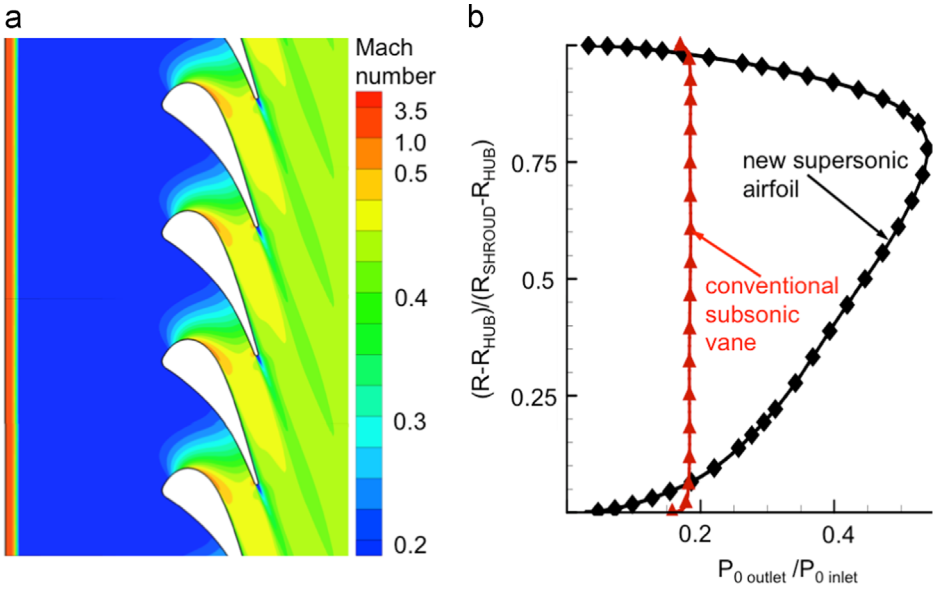

Fig. 13. Comparison with the NGV of [21]: a) Mach number contours exposed to the inlet conditions of Table 1; b) distributions of outlet to inlet total pressure ratio.

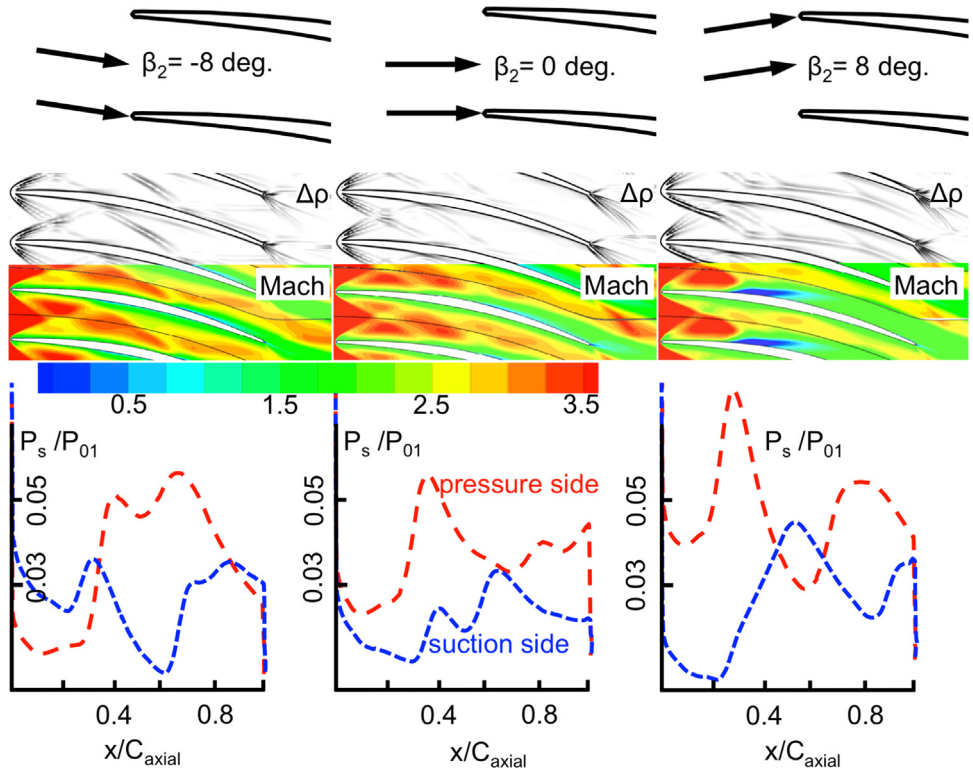

Fig. 14. Schlieren, iso-Mach number contours and static distribution on the rotor passage at three different inlet flow angles.

3.4. Grid sensitivity analysis

A grid independence study has been performed in order to estimate the numerical uncertainty of the present simulations. For this purpose, the Grid Convergence Index (GCI) method, described by Celik et al. [20], was considered. From the computational grid previously mentioned (so-called medium), one coarse grid and one fine grid were generated, keeping the grid refinement process structured and considering a grid refinement factor, r, recommended by the CGI method. Before performing the present analysis, iterative convergence has been demonstrated firstly by a decrease of at least five orders of magnitude in the normalized residuals for all the solved governing equations, and then by verifying that the net mass and energy imbalances were below 0.01%. Table 4 shows the main results obtained for the present grid sensitivity investigation for three quantities of interest: total pressure ratio ($P_{0\ outlet}/P_{0\ inlet}$), Mach number ($M_{outlet}$) and static pressure ($P_{s\ outlet}$). These quantities are mass flow-weighted average at a plane of constant axial position located at a distance of 50% of airfoil chord downstream from the trailing edge. The values of a quantity of interest (ϕ_{fine}, ϕ_{medium}, and ϕ_{coarse}) obtained with the three computational grids (N_{fine}, N_{medium}, and N_{coarse}) allowed one to predict the apparent order of accuracy (p) of the method, so that an extrapolated value ($\phi_{extrapolation}$) could be calculated. The highest numerical uncertainty in the fine-grid solution is observed for the ratio $P_{0\ outlet}/P_{0\ inlet}$, with an approximate relative error ($e_a^{\text{medium-fine}}$) of 2.6% and an extrapolated relative error ($e_{extrapolation}^{\text{medium-fine}}$) of 0.69%. The fine grid convergence index is a parameter that gives an estimation of the discretization uncertainty. This value is commonly defined by

$$GCI_{fine}^{medium-fine} = 1.25\left|\frac{\varphi_{ext}^{medium-fine} - \varphi_{fine}}{\varphi_{fine}}\right| \tag{21}$$

about 0.87% for the total pressure, and 0.66% for the Mach number, which is below typical experimental uncertainties. The effect of the grid size on the airfoil loading is shown in Fig. 11b. For the three considered grids there is only a slight variation in the static pressure at the impact of the leading edge shocks, on the pressure and suction side.

4. Aerodynamic results and discussion

4.1. Aerodynamic performance of the supersonic passage

The numerical Schlieren visualization displayed in Fig. 11a illustrates the complex shock patterns across the turbine passage. The two oblique shock waves generated at the leading edge interact with the boundary layers of the neighboring airfoils, and are reflected multiple times further downstream. Fig. 11b depicts the static pressure distribution along the airfoil, which is characterized by the strong fluctuations on the pressure and suction side imposed by the impact of the direct and reflected shock waves.

Fig. 12a shows the distortion in the Mach number field generated by the leading-edge shocks. Due to the passage area reduction and pressure losses, the passage outlet Mach number is reduced to 2.15, while the isentropic prediction (Table 2) stated a value of 3.4. The leading edge shocks and their interactions with the airfoil boundary layer cause substantial total pressure losses along the turbine. Fig. 12b presents the abatement of the total pressure across the passage, which is particularly apparent downstream of the airfoils trailing edges. Near the end-walls, extremely high total pressure losses were registered, in the boundary layers and vortical structures occurring in those regions. Moving towards the mid-span, total pressure losses are reduced, due to the decreased importance of secondary flows. $P_{0\ outlet}/P_{0\ inlet}$ reaches its maximum mass-weighted average value of 54% at a normalized radius $(R-R_{hub})/(R_{tip}-R_{hub})$ of approximately 0.78. At the outlet section of the computational domain, the mass flow-weighted averaged value for $P_{0\ outlet}/P_{0\ inlet}$ is 34%. This may appear to be low, however if one would expose a conventional turbine passage

(designed for an axial subsonic inlet flow) to an inlet axial Mach number of 3.5, the situation would be further deteriorated.

Fig. 13a shows the results of the steady Navier–Stokes simulations performed for a conventional nozzle-guide-vane (NGV), experimentally and numerically investigated at the von Karman Institute [21]. Due to the large contraction ratio of the NGV, $A_{throat}/A_{inlet} \approx 0.3$, the supersonic inlet flow is unstarted and a strong normal shock wave is established upstream of the turbine. Fig. 13b compares the total pressure loss of the conventional subsonic vane with the new supersonic airfoil. The new profile performs nearly twice better than the subsonic design.

4.2. Statorless inlet supersonic turbine analysis

The performance of a statorless turbine was numerically assessed considering as a rotor the turbine passage previously designed. The relative inlet angle, at design conditions, is zero, but we studied eight other off-design cases, with a variation in β_2 $\pm 8^\circ$. In all cases we considered identical relative inlet total pressure (40 bar), inlet relative Mach number 3.5, and that the rotor turns at 12,910 RPM, resulting in $U_2 = 500$ m/s. Hence, the total inlet conditions in the absolute frame of reference (P_{01} and T_{01}) increase with the relative inlet angle.

Fig. 14 evaluates the pressure distribution on the turbine passage with the aid of Schlieren and iso-Mach number contours, at negative incidence (left column), design (central column), and positive incidence (right column). At negative incidence ($\beta_2 = -8$) there are two concurrent effects. Firstly, the acceleration along the pressure side (in red) is enhanced, and consequently negative loading is observed in the front part of the airfoil. This is coupled with a weak right-running leading edge shock. At about 35% of the axial chord the left-running shock from the neighboring leading edge impacts on the pressure side, increasing the loading substantially above the suction side level. At around 25% of the axial chord the weak right-running shock from the other neighboring leading edge impacts on the suction side. By contrast, the strong leading-edge left-running shock is reflected on the pressure side, and then impacts again on the suction side at about 65% of the axial chord. Consequently, the pressure levels at the suction side approaches the value at the pressure side; such low difference creates a weak trailing edge right running shock [22]. At positive incidence angles ($\beta_2 = -8$), the effects at the leading edge are reversed, i.e. a steeper acceleration along the suction side (in blue) is coupled with a strong right-running leading edge shock. This intense right-running shock impacts on the suction side at about 30% of the axial chord, originating a bubble of recirculating flow that is clearly identified by the blue region in the iso-Mach contour. This separation region is eventually reattached to the suction side, and from 50% of the axial chord, the flow is again accelerated along the suction side.

Fig. 15a shows the incoming streamlines within the endwall's boundary layer being pushed first towards the suction side, and then upwards due to the combined effect of the main passage vortex, horse shoe vortex and shock waves. Therefore, the total pressure is severely diminished near the endwalls due to the secondary flows. The rotor pressure ratio P_{03R}/P_{02R} along the radial direction, shown in Fig. 15b, shows that additionally at positive incidence there is a net reduction in outlet total pressure, caused by the separation bubble present at positive incidence angles. Fig. 15c reveals an optimal massflow averaged relative total pressure (0.40) at about -2° of incidence, with a sheer drop of total pressure ratio at positive incidence angles (0.31 at about 8° of incidence). In Fig. 15d we observe that the flow angle is quenched through the turbine passage, at negative incidence angles the variation of outlet flow angle (β_3) is less than a degree. However, at positive incidence, due to the presence of the separation bubble, the outlet relative angle decays 3°. Fig. 15d also shows that the turbine outlet tangential component of the absolute velocity is barely sensitive to the change of incidence angle. An inlet tangential velocity ($V_{2,tangential}$) variation of around 400 m/s is associated to a maximum change of about 70 m/s in $V_{3,tangential}$. Therefore, the turbine power (Fig. 15c) follows the same trend of $V_{2,tangential}$, based on the Euler equation Eq. (21). At design conditions ($\beta_2 = 0^\circ$) the produced power is 16.4 MW, for a turning

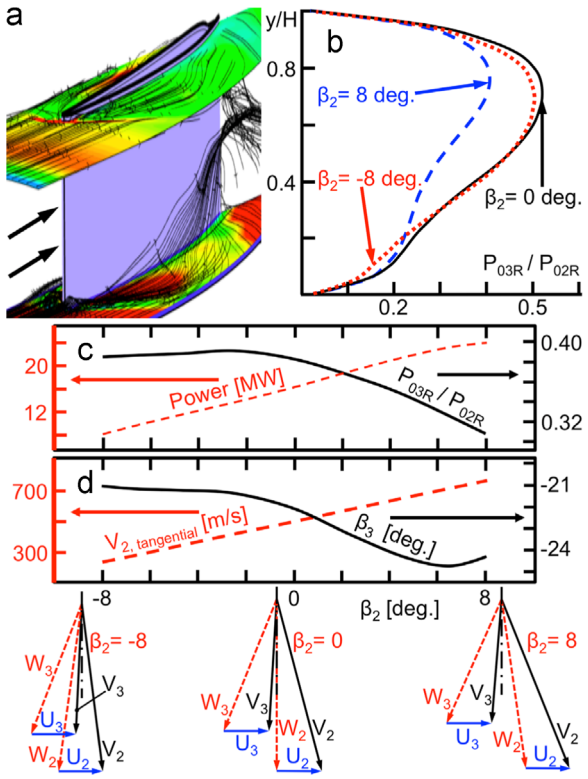

Fig. 15. (a) 3D visualization of the secondary flows developing along the suction side; b) Radial distribution of the total pressure ratio; c) Massflow averaged total pressure losses and power; d) Tangential velocity, outlet flow, and the velocity.

Table 5
Statorless turbine inlet and outlet conditions.

	β_2 [deg]	−8	0	+8
2	P_{02} [bar]	39	47	56
	P_{02R} [bar]	40	40	40
	P_{s2} [bar]	0.52	0.52	0.52
	T_{s2} [K]	725	725	725
	α_2 [deg]	7.2	14.8	22.2
	V_2 [m/s]	1885	1954	2020
	W_2 [m/s]	1889	1889	1889
	U_2 [m/s]	500	500	500
	ω [m/s]	12910	12910	12910
	M_{02R} [−]	3.5	3.5	3.5
	$\dot{m}$[kg/s]	54.9	55.3	54.9
3	P_{03} [bar]	10.3	10.2	8.5
	P_{03R} [bar]	15.3	15.3	12.3
	P_{s3} [bar]	1.19	1.19	1.40
	T_{s3} [K]	1261	1255	1380
	α_3 [deg]	−2.5	−3.6	−4.8
	β_3 [deg]	−21.1	−22.1	−24.3
	V_3 [m/s]	1466	1460	1366
	W_3 [m/s]	1568	1572	1492
	U_3 [m/s]	500	500	500
	M_{03R} [−]	2.24	2.25	2.02

of roughly 20° .

$$\frac{Power}{\dot{m}} = U_2 \cdot V_{2,\ \tan\ gential} - U_3 \cdot V_{3,\ \tan\ gential} \quad (21)$$

Table 5 summarizes the thermodynamic parameters at the inlet and outlet sections of the statorless turbine, for three different relative flow angles. The turbine rotor outlet Mach number decreases across the passage due to the diffusion and shock waves. At positive incidence the downstream Mach number is minimum due to the separation bubble. Both static pressure and temperature increase across the passage, due to the diffusion.

4.3. Analysis of the transient supersonic starting process

The turbine passage was then submitted to a sudden transition from a subsonic flow to a high supersonic flow to evaluate the performance under highly variable conditions, representative of the cyclic generation of normal shock waves upstream of the turbine. The unsteady simulation was initiated from a converged solution obtained at subsonic conditions. Fig. 16a shows the flow performance at successive temporal instants. At first the normal shock is upstream of the passage, hence the flow is subsonic. In the second image the normal shock is approaching the leading edge, and we observe how oblique shocks start to develop. One can visualize the generation of recirculation regions on the suction side. As the normal shock is being ingested, the full development of the oblique shock–boundary layer interactions is observed, until stable supersonic conditions are achieved at the passage exit. The flow required approximately 27 ms to ingest the normal shock waves and become stabilized.

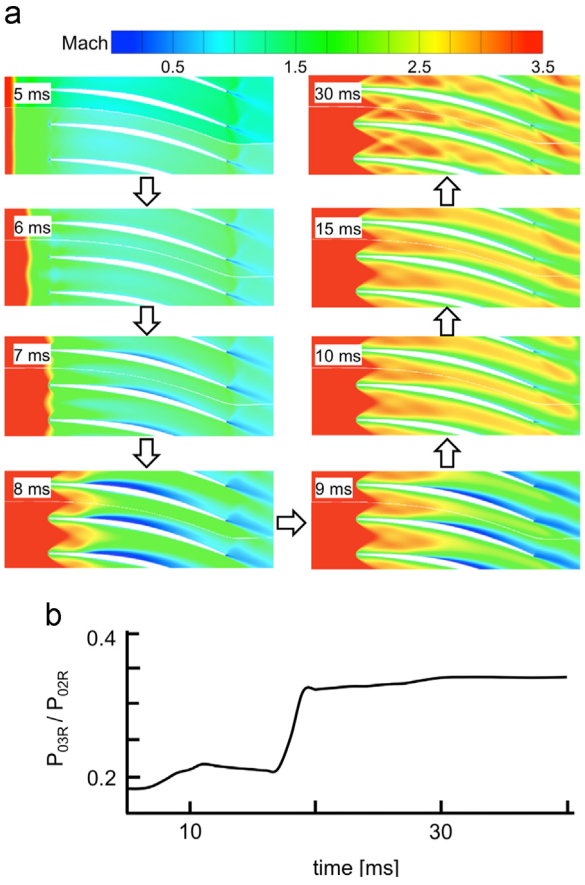

Fig. 16. a) Time-resolved performance of the passage during the starting phase; b) Temporal evolution of the ratio of relative total pressure across the rotor passage.

Fig. 16b shows the instantaneous ratio of relative inlet pressure to relative outlet pressure, these values were massflow averaged. During this transient P_{02R} remains constant, hence the large deficit of total pressure occurring at the initial part of the transient process is due to the time that the flows requires to be established. Once the normal shock enters the rotor passage (at about 8 ms) the outlet pressure raises about 50%.

5. Conclusions

Current research on groundbreaking thermodynamic cycle's has shown an unacceptable performance of the conventional turbine devices. The present research has shown that conventional subsonic turbine designs are inadequate for supersonic conditions, due to the generation of an intense normal shock wave at the inlet. The proposed supersonic passages were designed using a methodology based on the method of characteristics. The turbine passage is comprised of three zones which, (i) convert the uniform parallel flow at the passage inlet into a vortex flow field, (ii) turn the vortex flow, and (iii) reconvert it into a uniform parallel flow at the airfoil exit. Several airfoil geometries were designed with varying exit Mach numbers.

The proposed design procedure has been assessed using three-dimensional Navier–Stokes simulations. The computational grid was first carefully selected to ensure a grid independent solution based on the CGI method. The simulations comprised steady and unsteady-transient analysis. The results showed the ability of the present design to ingest normal shock waves, allowing the passage to operate in the supersonic regime. Furthermore, the coupled analysis of the density gradient contours together with the pressure losses revealed the prime source of loss attributed to the leading edge shock reflections across the turbine passage. The developed design tool allows producing turbine passages twice more efficient than the current state-of-the-art turbine designs.

The aerodynamic performance of a statorless turbine was analyzed at several incidence angles. Severe pressure abatement is observed due to shock losses and secondary flows. At high incidence, a separation bubble on the suction side creates significant losses. In contrast to subsonic turbines the static pressure increases along the turbine. In spite of the limited turning, large values of power are extracted. Furthermore, the starting phase from stagnation to supersonic regime was analyzed with a transient simulation, complex shock patters develop during the ingestion of normal shock waves, which typically last for about 30 ms.

Fluid machinery designers are usually constrained to operate in the subsonic regime, however the present design approach opens avenues for the development of revolutionary ultra compact power generation concepts.

Acknowledgments

The authors would like to acknowledge Oscar Martinez Moralo for his work regarding the off-design performance of the turbine passage and John McClean for his advise during the preparation of the final manuscript.

References

[1] Ghigliazza F, Traverso A, Massardo AF. Thermoeconomic impact on combined cycle performance of advanced blade cooling systems. Appl Energy0306-2619 2009;86:2130–40. http://dx.doi.org/10.1016/j.apenergy.2009.01.023.
[2] Thyssen-Holzwarth oil and gas turbines. J. Am. Soc. Naval Eng. 1922;34 (3):453–7 (August).

[3] Roy GD, Frolov SM, Borisov AA, Netzer DW. Pulse detonation propulsion: challenges, current status, and future perspective. Prog Energy CombustSci0360-1285 2004;30(6):545–672. http://dx.doi.org/10.1016/j.pecs.2004.05.001.
[4] Van Zante, D, Envia, E, and Turner, M G, 2007, The attenuation of a shock wave by an aircraft engine axial turbine stage, In: Proceedings of the International Symposium on Airbreathing Engines, Paper 2007-1260, Beijing, China, September.
[5] Galindo J, Fajardo P, Navarro R, García-Cuevas LM. Characterization of a radial turbocharger turbine in pulsating flow by means of CFD and its application to engine modeling. Appl Energy0306-2619 2012;103:116–27. http://dx.doi.org/10.1016/j.apenergy.2012.09.013.
[6] Verneau, A, 1987, Supersonic Turbines for Organic Fluid Rankine Cycles from 3 to 1300 kW, Verdonk, G., and Dufournet, T., Development of a Supersonic Steam Turbine with a Single Stage Pressure Ratio of 200 for Generator and Mechanical Drive, von Karman Institute Lecture Series on "Small High Pressure Ratio Turbines", June.
[7] Wahlen, U, 1999, The aerodynamic design and testing of a supersonic turbine for rocket engine application, In: Proceedings of the 3rd European Conference on Turbomachinery, London, United Kingdom, March.
[8] Grönman A, Turunen-Saaresti T, Jaatinen A, Backman J. Numerical modelling of a supersonic axial turbine stator. J Therm Sci1003-2169 2010;19(3):211–7. http://dx.doi.org/10.1007/s11630-010-0211-5.
[9] Goldman LJ, Vanco MR. Computer Program for Design of Two-Dimensional Sharp-Edged-Throat Supersonic Nozzles with Boundary-Layer Correction. NASA Technical Memorandum, TM X-2343, Published by National Aeronautics and Space Administration, Lewis research center, Cleveland, Ohio.
[10] A.J. Glassman, Turbine Design and Application, NASA SP-290, 1972, Published by National Aeronautics and Space Administration, Lewis research center, Cleveland, Ohio.
[11] Shapiro A. The dynamics and thermodynamics of compressible fluid flow. The Ronald Press Company; ISBN: 9780471066910. John Wiley & Sons Inc. 1953.
[12] Boxer E, Sterret JR, Wlodarski J. Application of supersonic vortex-flow theory to the design of supersonic impulse compressor - turbine blade sections. NACA Research Memorandum L52B06. Published by the National Advisory Committee for Aeronautics. Langley Aeronautical Laboratory, Langley Field, Virginia. (NACARM52B06).
[13] Goldman LJ, Scullin VJ, 1968, Analytical Investigation of Supersonic Turbomachinery Blading I - Computer Program for Blading Design, NASA Technical note TN D-4421. National Aeronautics and Space Administration, Lewis Research Center, Cleveland, Ohio.
[14] Kantrowitz A, Donaldson CD. Preliminary Investigations of Supersonic Diffusers. (NACA Report ACR-L5D20). Langley Field, VA: Langley Memorial Aeronautical Laboratory; 1945.
[15] Colclough CD. Design of turbine blades suitable for supersonic relative inlet velocities and the investigation of their performance in cascades: part I-theory and design. J Mech Eng Sci 1966;8(1):110–28.
[16] Joly M, Verstraete T, Paniagua G. Multidisciplinary design optimization of a compact highly-loaded fan. Structural and Multidisciplinary Optimization. Journal of the International Society for Structural and Multidisciplinary Optimization. Published online: 25 August 2013. StructMultidiscOptim1615-147X2013. http://dx. doi.org/10.1007/s00158-013-0987-5 (August).
[17] Goldberg U, 2011, Subsonic and Transonic External Aerodynamics: CFD++ Capabilities and Verification. Technical report, Metacomp Technologies.
[18] Haas A, 2010, Assessment and validation of intermittency transport equations for modelling hypersonic transition with CooldFluid and CFD++, Technical report, von Karman Institute for Fluid Dynamics Project report VKI 2010–15, June. von Karman Institute for Fluid Dynamics, Rhode Saint Genese, Belgium.
[19] Smith HE. Experimental and theoretical investigation of the near wake behind a rearward facing step in supersonic flow. (PhD Dissertation). University of Cincinnati; 1969.
[20] Celik IB, Ghia U, Roache PJ, Freitas CJ, Coleman H, Raad PE. Procedure for estimation and reporting of uncertainty due to discretization in CFD applications. ASME J Fluids Eng 0098-2202 2008;130(078001):4. http://dx.doi.org/10.1115/1.2960953 (pages).
[21] Paniagua G, Yasa T, de la Loma A, Castillon L, Coton T. Unsteady strong shocks interactions in a transonic turbine: experimental and numerical analysis. J Propul Power0748-4658 2008;24(4):722–31. http://dx.doi.org/10.2514/1.34774, July–August0748-4658 2008. http://dx.doi.org/10.2514/1.34774.
[22] Joly M, Verstraete T, Paniagua G. Differential evolution based soft optimization to attenuate vane-rotor shock interaction in high-pressure turbines. Appl Soft Comput1568-4946 2013;13(4):1882–91. http://dx.doi.org/10.1016/j.asoc.2012.12.005 (April).